



Delft University of Technology

## Operando Topography and Mechanical Property Mapping of CO<sub>2</sub> Reduction Gas-Diffusion Electrodes Operating at High Current Densities

Nesbitt, Nathan T.; Smith, Wilson A.

**DOI**

[10.1149/1945-7111/abf183](https://doi.org/10.1149/1945-7111/abf183)

**Publication date**

2021

**Document Version**

Final published version

**Published in**

Journal of the Electrochemical Society

**Citation (APA)**

Nesbitt, N. T., & Smith, W. A. (2021). Operando Topography and Mechanical Property Mapping of CO<sub>2</sub> Reduction Gas-Diffusion Electrodes Operating at High Current Densities. *Journal of the Electrochemical Society*, 168(4), Article 044505. <https://doi.org/10.1149/1945-7111/abf183>

**Important note**

To cite this publication, please use the final published version (if applicable).

Please check the document version above.

**Copyright**

Other than for strictly personal use, it is not permitted to download, forward or distribute the text or part of it, without the consent of the author(s) and/or copyright holder(s), unless the work is under an open content license such as Creative Commons.

**Takedown policy**

Please contact us and provide details if you believe this document breaches copyrights.

We will remove access to the work immediately and investigate your claim.

OPEN ACCESS

## Operando Topography and Mechanical Property Mapping of CO<sub>2</sub> Reduction Gas-Diffusion Electrodes Operating at High Current Densities

To cite this article: Nathan T. Nesbitt and Wilson A. Smith 2021 *J. Electrochem. Soc.* **168** 044505

View the [article online](#) for updates and enhancements.

The Electrochemical Society  
Advancing solid state & electrochemical science & technology

**239th ECS Meeting with IMCS18**

DIGITAL MEETING • May 30-June 3, 2021

Live events daily • Access for free

18th

Register now!



# Operando Topography and Mechanical Property Mapping of CO<sub>2</sub> Reduction Gas-Diffusion Electrodes Operating at High Current Densities

Nathan T. Nesbitt<sup>1,2,z</sup>  and Wilson A. Smith<sup>1,2,3,z</sup> 

<sup>1</sup> Materials for Energy Conversion and Storage, Department of Chemical Engineering, Delft University of Technology, 2629 HZ Delft, The Netherlands

<sup>2</sup> Materials, Chemical, and Computational Science (MCCS) Directorate, National Renewable Energy Laboratory, Golden, CO 80401, United States of America

<sup>3</sup> Renewable and Sustainable Energy Institute (RASEI) and Department of Chemical and Biological Engineering, University of Colorado Boulder, Colorado 80303, United States of America

Electrochemical atomic force microscopy (EC-AFM) enables measurement of electrode topography and mechanical properties during electrochemical reactions. However, for aqueous-based reactions that make gas products, such as CO<sub>2</sub> reduction and water splitting into CO/H<sub>2</sub>, current densities below 1 mA cm<sup>-2</sup> have been necessary to prevent formation of bubbles at the electrode; such bubbles can stick to the AFM probe and prevent further AFM imaging. Here, we demonstrate a novel cell design with a gas-diffusion electrode (GDE) to exhaust the gas products, thereby enabling high current density EC-AFM measurements at 1, 10, and 100 mA cm<sup>-2</sup> that are not disturbed by bubble formation at the electrode surface. These experiments revealed a stable morphological structure of Cu catalysts deposited on GDEs during high current density operation. Systematic spatially resolved maps of deformation and adhesion showed no signs of a gas-liquid interface between catalyst particles of the GDE.

© 2021 The Author(s). Published on behalf of The Electrochemical Society by IOP Publishing Limited. This is an open access article distributed under the terms of the Creative Commons Attribution 4.0 License (CC BY, <http://creativecommons.org/licenses/by/4.0/>), which permits unrestricted reuse of the work in any medium, provided the original work is properly cited. [DOI: [10.1149/1945-7111/abf183](https://doi.org/10.1149/1945-7111/abf183)]



Manuscript submitted November 3, 2020; revised manuscript received March 18, 2021. Published April 7, 2021.

Supplementary material for this article is available [online](#)

Electrochemical atomic force microscopy (EC-AFM) is a well-developed technique that enables topography measurements of electrode surfaces during electrochemical reactions. Its main defining features are a sample holder and probe holder that allow the AFM probe and sample to be immersed into an electrolyte, and an electric potential applied between the sample and a counter electrode while the AFM scans the sample surface. AFM tapping modes that record a pseudo-force curve upon each oscillation have been developed in recent years by several AFM companies, allowing for simultaneous mechanical property mapping during topography measurements<sup>1</sup> (PeakForce-tapping by Bruker, Inc.,<sup>2</sup> Fast Force Mapping by Asylum Research, Inc.). These properties include tip-sample adhesion force and sample deformation displacement.

EC-AFM is a valuable technique because it provides quantitative operando topography and spatial maps of adhesion, deformation, reduced Young's modulus,<sup>3</sup> and other mechanical properties.<sup>4</sup> In combination with specialty probes, it can enable microscopic investigation of a wide range of surface properties such as electric potential,<sup>5,6</sup> surface charge,<sup>5</sup> and electrochemical strain.<sup>7,8</sup> EC-AFM also spans a wide range of resolutions: AFM tips typically have a radius of ~5 nm that allow detailed 256 × 256 pixel images of scan size as small as ~1 μm, while the piezo-electric scanners of AFMs typically have a maximum scan size of 10–100 μm.

Operando measurements are valuable for understanding electrochemical systems because pre- and post-mortem measurements made before and after a potential is applied to a catalyst cannot determine catalyst structure *while* the potential is applied. When a potential is applied to an electrode to drive an electrochemical reaction, the electrode can restructure from the changing electric potential or microenvironment, or be coated by precipitates, but such developments can be obscured by further changes when the potential is turned off.<sup>9–14</sup> In EC-AFM, an electrode may have different topography and mechanical properties while an electric potential drives a reaction than it did before or after the potential was applied. Even if turning off the applied potential is not expected to further modify a catalyst, EC-AFM makes it practical to measure

topography evolution upon repeated cycling of the electric potential.<sup>15,16</sup> While we are not considering here either electrochemical atomic-resolution AFM<sup>17</sup> or electrochemical scanning tunneling microscopy (EC-STM),<sup>18,19</sup> techniques that could offer explicit measurement of surface arrangement of atoms at crystalline surfaces but require pristine atomically flat samples, the catalyst geometry measured by nano and micro-scale EC-AFM can also offer insights into likely changes in catalyst surface faceting, agglomeration, or degradation.<sup>10,15,20</sup>

For aqueous reactions that make gaseous products, such as CO<sub>2</sub> reduction into CO, these measurements have been constrained to low current densities ( $\leq 1 \text{ mA cm}^{-2}$ ) for which the gas products can remain dissolved in the electrolyte<sup>13,14</sup>; otherwise, bubbles form at the electrode, stick to the AFM probe, block the laser path between AFM probe and photodiode, and prevent further AFM imaging. We are only aware of one pseudo-operando EC-AFM study of CO<sub>2</sub>R catalysts, which probed the surface after potential pulses.<sup>4</sup> Here we demonstrate that with proper cell design, a gas-diffusion electrode (GDE) will allow gas products to leave through the diffusion media, thereby leaving an unobstructed catalyst surface and enabling high current density EC-AFM measurements.

## Experimental

**Sample preparation.**—Two layers of Tesapack® Strong Transparent (tesapack) tape from Tesa, Inc. (45 μm thick, bi-axially oriented polypropylene (BOPP) backing material with acrylic adhesive) were adhered to a layer of Tesa® Extra Power Transparent (tesaEPT) tape from Tesa, Inc. (140 μm thick, polyethylene film backing material with acrylic adhesive), which was adhered to a clean acrylic plate. The tesaEPT layer was included because, if the top two layers were adhered directly to materials like the acrylic plate or a glass slide, then the adhesive would peel from the BOPP backing. However, removal of tesapack from the tesaEPT tape backing always maintained the tesapack tape's integrity. A steel razor was used to cut a 10 × 10 mm square in the tape layers, and a steel leather-hole-punch of 0.5 or 1 mm diameter with a small mallet was used to punch a hole in the tape at the center of the square. The razor was used to lift a corner of the top tape layer and fold it under itself for easy access later. A pipette was used to deposit a droplet of

<sup>z</sup>E-mail: [nathan.nesbitt@nrel.gov](mailto:nathan.nesbitt@nrel.gov); [wilson.smith@nrel.gov](mailto:wilson.smith@nrel.gov)

0.1 M sulfuric acid onto each circular hole to dissolve any deposits of steel (i.e. Ni or Fe) left by the hole punch. After 1–2 min, the sulfuric acid was rinsed away with de-ionized water. Note, scotch tape cannot be supplemented for any tape layers because the sulfuric acid was found to degrade it.

A Sigracet 39bc gas-diffusion layer (GDL) sheet was cut into  $4 \times 4$  mm pieces. A glass slide was prepared with a layer of tesaEPT tape. The GDL pieces were placed on the tape layer at  $\sim 15$  mm spacing with the microporous layer facing up (matte finish side). One of the double-layered squares of tesapack tape was adhered to each GDL piece, with the circular hole centered on the GDL (Fig. A-1a). These were mounted to sputter plates, and  $100+/-5$  nm of Cu, Ag, or Au were deposited onto the GDL to form a GDE. The top layer of tesapack tape was carefully lifted from the bottom layer (Fig. A-1b), leaving the GDL within the circular opening of the bottom tape layer as the only part sputtered by a metal film (Fig. A-1c). Care was taken to ensure the bottom tape layer did not peel from the GDL while the top tape layer was removed. These samples were carefully peeled from the tesaEPT layer on the glass slide, and placed on the base of the electrochemical cell, as depicted in Figs. 1a–1c.

**Electrochemical cell design.**—The electrochemical cell was a modification of the Bruker Icon electrochemical cell for EC-AFM and atomic force microscope—scanning electrochemical microscopy (AFM-SECM). The only change was the addition of a 6 mm thick plastic insert (PEEK) between the electrochemical cell stainless steel base plate and the electrolyte. The insert is the bottom-most component of the electrochemical cell shown in Fig. 1a and is shown schematically in Fig. 1c as the only PEEK component. This insert had a 1 mm thick flat top-surface above a cylindrical cavity of  $\sim 30$  mm diameter and 5 mm height. There were fittings on the sides of the insert for gas inflow and outflow to and from the cavity. A 1 mm diameter circle was drilled through the top-surface from the cavity to the sample mount position. The top of the PEEK was coated by a layer of Al tape with a 2 mm hole centered on the hole in

the PEEK. The Al was coated by a layer of tesaEPT tape for electrical insulation. The tesaEPT tape had a  $5 \times 5$  mm<sup>2</sup> square hole centered on the hole in the Al. GDE samples were placed in this square opening with the carbon paper in contact with the Al tape, which was connected to a potentiostat (CH Instruments, Inc. 760E).

**Vacuum and water bubbler vial.**—To create a slight negative pressure on the gas side of the GDE during  $100 \text{ mA cm}^{-2}$  electrolysis, a 20 ml glass vial with open-top septa cap was filled half-way with water. A syringe needle connected to the gas outflow of the electrochemical cell punctured the septa to the vial head-space. A second syringe needle open to atmosphere punctured the septa and was immersed  $\sim 1.5$  cm below the water surface. A third syringe needle connected to a vacuum pump punctured the septa to the vial head-space. Thus, the gas pressure below the GDE was less than atmospheric pressure by the pressure of 1.5 cm of water ( $\sim 150$  Pa).

**Electrochemical cell build.**—The GDE was most easily placed on the electrochemical cell base with the cover glass removed. To seal the cell, the cover glass was slid into position, the top screws tightened cross-wise until a thin line of contact was apparent against the O-ring, and then the bottom screws tightened to seal the bottom plate to the cell sidewalls. Overtightening would easily break the brittle and expensive fused-silica cover glass.

**Electrolyte preparation.**—0.1 M  $\text{KHCO}_3$  electrolyte solution was prepared by mixing powdered  $\text{KHCO}_3$  with de-ionized water ( $18 \text{ M}\Omega$ ) and deaerating the electrolyte with a plastic 10 ml syringe. Deaerating ensured small temperature changes would not cause gas bubble nucleation on the GDE or AFM probe.

**Cell initialization.**—The custom insert that allowed gas flow below the GDE had 1 sccm of  $\text{CO}_2$  flowed through it for 10–30 min prior to filling the cell with electrolyte to ensure atmospheric air ( $\text{N}_2$  and  $\text{O}_2$ ) are exhausted from the cell.  $\text{CO}_2$  flow would be continued at 1 sccm for 30–60 min before electrolysis was started.

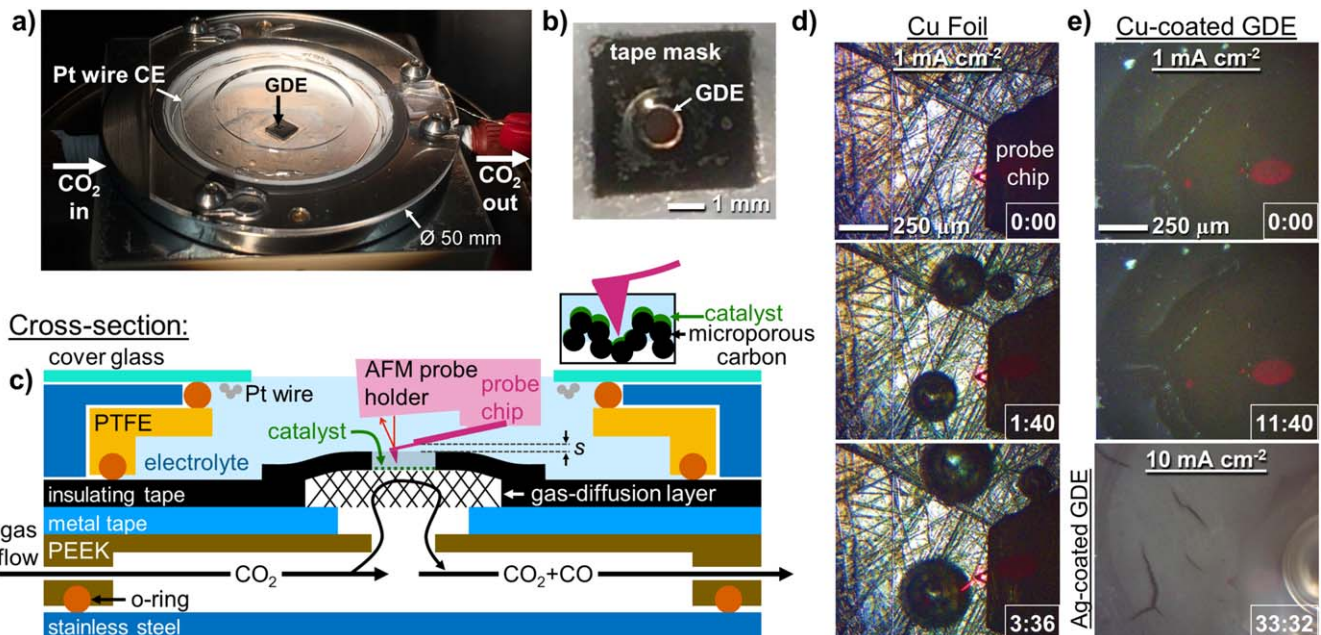


**Figure 1.** EC-AFM electrochemical cell schematic and photos, demonstrating bubbles formation on foil and not on a GDE. (a) Photo of the electrochemical cell. (b) Photo of the Cu-sputtered GDE with a polypropylene mask. (c) Cross-sectional schematic of the electrochemical cell: the AFM cantilever is the thin line extending from the probe chip;  $s$  denotes the separation between the probe and tape mask; the O-ring seal against the insulating tape is 36 mm diameter; inset shows magnified view of microporous carbon sputter-coated by catalyst and probed by an EC-AFM. (d) Photos of a Cu foil, demonstrating formation of large bubbles at  $1 \text{ mA cm}^{-2}$  from 0 to 3 min 36 s. The pink/brown coloration is the tape mask with 1 mm diameter opening. (e) (top-middle) Photographs of Cu-sputtered GDEs with 0.5 mm diameter at  $1 \text{ mA cm}^{-2}$  show absence of bubbles at 0 min and 11 min 40 s. (bottom) Ag-sputtered GDE with 1 mm diameter at  $10 \text{ mA cm}^{-2}$  shows detailed GDE surface at 33 min 32 s of electrolysis; Ag below tape mask caused bubbles at mask edge that accumulated on top of AFM chip but in this instance did not block laser path (Ag is more reflective than Cu, allowing detailed photograph).

**EC-AFM measurements.**—A CHI 760E potentiostat was connected to a Pt wire counter electrode and the GDE working electrode. A two electrode setup was used, so the reference electrode lead of the potentiostat was connected to the Pt wire counter electrode. After checking the sample position in air (x,y,z position on Bruker Icon stepper motors), a flexible plastic pipette was used to fill the electrochemical cell with 2 ml of electrolyte. To ensure no leak of electrolyte caused an electrical short between the GDE and counter electrode, electrochemical impedance between the GDE and Pt wire was recorded at 100 Hz while the electrochemical cell was filled with electrolyte and the EC-AFM was submerged in electrolyte and engaged with the GDE. Typical impedance magnitude ( $|Z|$ ) without electrolyte was  $10^8 \Omega$ . Typical  $|Z|$  with electrolyte was  $10^4 \Omega$ . A lower  $|Z|$  or a change in  $|Z|$  not timed with the electrolyte first contacting the GDE and Pt wire were tell-tale signs of an electrical short. With the EC-AFM submerged in electrolyte and probe engaged with the GDE, impedance measurements were ended, and 0 mA cm<sup>-2</sup> EC-AFM scans recorded. Subsequently, chronopotentiometry (CP) was used to apply 1, 10, or 100 mA cm<sup>-2</sup> between the GDE and Pt wire. PeakForce (PF) tapping in the Quantitative Nanomechanical Mapping workspace of the Bruker Icon was used at PF tapping frequency 1 or 2 kHz.

## Results and Discussion

The main purpose of this report is to demonstrate a technique for operando EC-AFM measurements of catalysts while they perform electrocatalysis in an aqueous medium and produce gas at high current densities (1, 10, and 100 mA cm<sup>-2</sup>). Cu and Ag were used as catalysts due to their popularity in the electrochemical CO<sub>2</sub>R research field; their Faradaic efficiency for different products is assumed similar to that in literature.<sup>21–25</sup> It has not previously been

possible to study these catalysts under these conditions with EC-AFM due to the formation of gas bubbles, which can interrupt the path of the laser used for the AFM measurement (red laser is depicted in Fig. 1c between AFM probe holder and the AFM probe). As such, we begin with a discussion of important characteristics and challenges of the cell design (described in experimental section and depicted in Fig. 1), followed by an analysis of the EC-AFM data.

**Electrochemical cell.**—Bubble mitigation was the main challenge in this work and was possible to avoid by using a GDE working electrode. A GDE has diffusion media on the gas-fed side, composed of a macroporous carbon paper backing and a hydrophobic microporous carbon middle layer (diffusion media labeled in Fig. 1c as gas-diffusion layer).<sup>22</sup> On the liquid side of the GDE is a hydrophilic catalyst layer (green dashed line in Fig. 1c). The GDE allows gas reactants and products to diffuse a short distance to and from a catalyst immersed in liquid electrolyte.<sup>26</sup> Building a flow cell with a gas stream below the GDE allowed gas created by the reaction to exhaust from the cell through the GDE diffusion media (as in Fig. 1e) instead of forming gas bubbles in the electrolyte (as in Fig. 1d). Since commercial electrolyzers often use GDEs to enable high current density operation, this approach also allowed catalysts to be studied under commercially relevant conditions.

While the GDE provided a means to exhaust gaseous products and achieve large current densities, using a small electrode surface area kept overall current in the cell low, which improved overall cell stability. For this reason, GDEs were masked with tape to expose only a 0.5 to 1 mm diameter area of the GDE to the electrolyte; such a mask on a Cu-sputtered GDE is depicted in the photo of Fig. 1b (and in Fig. 1e mounted beneath the AFM probe). This small active GDE area ensured the surface area of the counter-electrode was

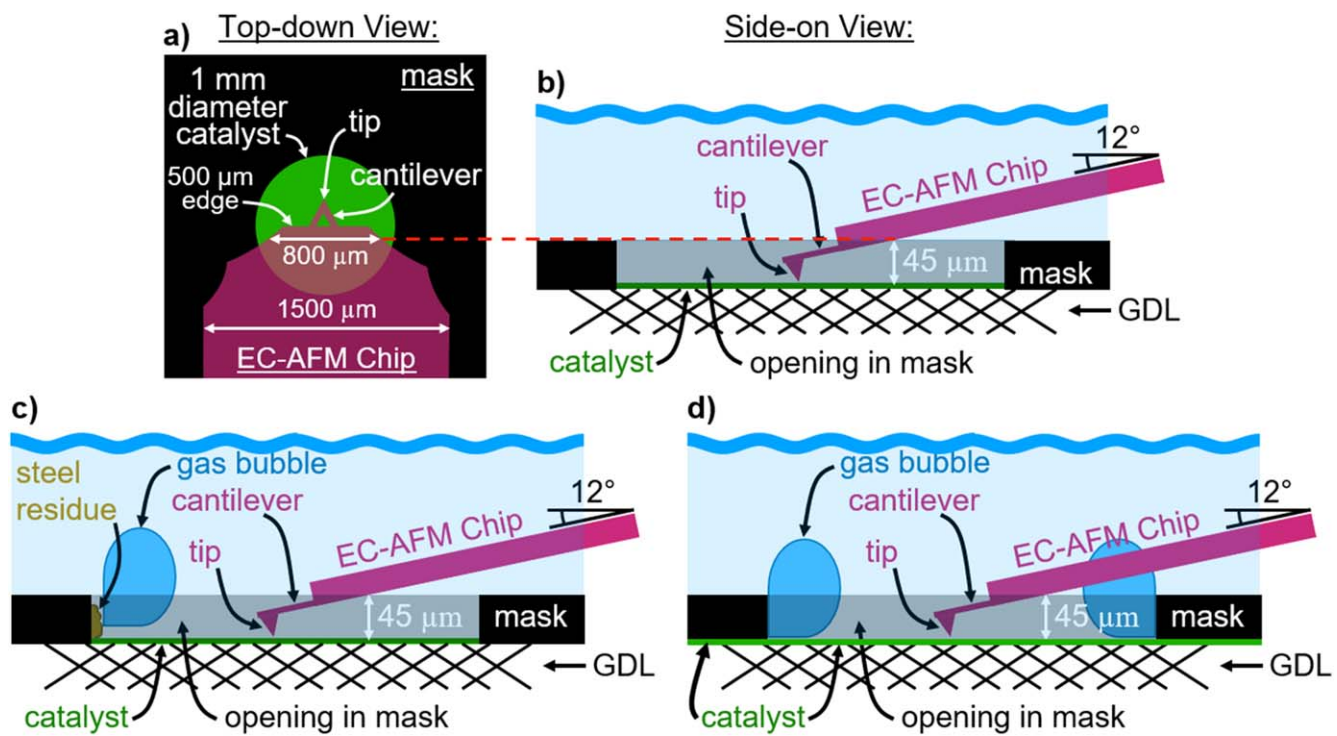


**Figure 2.** Schematic of AFM chip and probe over masked catalyst. (a) Top-down view shows how the width of the AFM chip compares with the width of the opening in the tape; dashed red line shows that where the AFM chip was 800  $\mu\text{m}$  wide, it was 45  $\mu\text{m}$  above the catalyst. (b) Side-view shows geometric constraints on the EC-AFM probe (Bruker ScanAsyst-Fluid+) reaching the catalyst surface through the 1 mm diameter 45  $\mu\text{m}$  deep opening in the tesapack tape mask. (c) Side-view shows the case of catalyst only in the opening of the mask, and how steel residue from the hole punch caused gas bubbles in the electrolyte. (d) Side-view shows the case of catalyst below the mask, and how this caused gas bubbles in the electrolyte.

much larger than the working electrode and ensured the distance between the counter electrode and GDE had little variation from the GDE center to GDE edge. The latter condition was important for relatively uniform current distribution on the GDE. The uniform current distribution and the small lateral distance between the catalyst and electrical contact of GDL to Al tape ensured ohmic drops did not cause spatial variation in the electric potential of the GDE.<sup>27</sup>

Lower ionic current in the electrolyte provided lower diffusion gradients (such as pH gradients) in the 2 ml of electrolyte in the cell, as well as a lower volume of O<sub>2</sub> gas produced at the Pt wire anode. Since this anode was immersed in the same electrolyte volume as the GDE, O<sub>2</sub> bubbles formed at the anode could diffuse through the electrolyte and stick to the AFM probe, blocking the probing laser path. This O<sub>2</sub> could also replace the desired reactant gas since the oxygen reduction reaction (ORR) had a less negative onset potential than HER or CO<sub>2</sub>R on the same cathode. Future work would benefit from a membrane placed between the cathode and anode to prevent O<sub>2</sub> diffusion to the cathode. However, anion exchange membranes (AEM) or cation exchange membranes (CEM) would cause accumulation of H<sup>+</sup> or OH<sup>-</sup>, respectively, in the catholyte. A bi-polar membrane (BPM) would avoid such accumulation and thus be preferred.

The setup used only two electrodes, the Pt wire anode and GDE cathode. This simplified the cell, which was of practical importance to minimize leaks during cell setup. Leaks of electrolyte typically required rebuilding the cell with a new sample. However, future work would benefit from the inclusion of a Ag/AgCl micro-reference electrode to more accurately identify reactions and their overpotential at the GDE, and correlate this to catalyst restructuring or degradation.<sup>11,12</sup>

The small area of the GDE exposed through the tape can result in the tape touching the AFM chip before the probe can reach the GDE surface. The point of least separation between the AFM chip and tape mask is labeled as separation *s* in Fig. 1c. The Bruker ScanAsyst Fluid + AFM probe used here had a chip that was 1500 μm wide, tapering down to 500 μm wide at the edge that the cantilever was mounted to (as shown in Fig. 2a). The cantilever length was 70 μm. The chip was mounted to the probe holder at 12° from the horizontal, so the cantilever descended a Δz of ~15 μm from the chip edge. The probe was nominally 2.5 to 8 μm tall. The tesapack tape used as a mask was 45 μm thick. For a 500 μm diameter opening in the tape, the chip will contact the tape before the probe reaches the GDE. In this case, the side edges of the chip were scraped away with tweezers to narrow the chip (depicted in photographs shown in Fig. 1d); no negative impact on AFM image quality was observed from the chip modification. For a 1000 μm diameter opening, the as-manufactured chip taper allowed the probe to reach the GDE surface; 211 μm from the probe contact point (2.5 μm tip height +15 μm cantilever Δz +27.5 μm chip Δz) the AFM chip reached the 45 μm clearance height. The chip was ~800 μm wide where it exited the tape mask hole (visible in bottom photo of Fig. 1e and shown schematically in Fig. 2b).

To demonstrate practical challenges to bubble mitigation, we discuss two circumstances in which gas bubbles would evolve into the electrolyte despite our utilization of a GDE. (1) A steel hole punch was used to cut a circular hole in a tape mask, through which the electrolyte could access the GDE. If the tape mask was not soaked in sulfuric acid following cutting of this hole, before adherence to the GDL, then bubbles would evolve from the edge of the tape, as depicted in Fig. 2c. This was likely H<sub>2</sub> gas produced by the HER as trace deposits of Ni or Fe may have been left by the hole punch. (2) If the catalyst (e.g. Cu, Ag, or Au) was deposited onto the entire 4 × 4 mm GDL, and the tape mask subsequently applied to the GDE, then bubbles would evolve into the electrolyte from the edges of the circular hole in the tape, as depicted in Fig. 2d, and could stick to the AFM probe. However, bubbles were unlikely

to evolve into the electrolyte at 1, 10, or 100 mA cm<sup>-2</sup> if the tape mask had two tape layers, the top layer as a removable sputter mask and the bottom layer as a permanent electrolyte mask to confine electrolyte-GDE contact to a small circular area. In this arrangement, the sputter mask allowed the catalyst to be deposited on the GDL only within the area exposed to electrolyte.

A trade-off of using GDEs to enable high current density EC-AFM measurements was their rough topography, which required a low tip velocity to maintain tip-sample contact. To have good temporal resolution on changes in the GDE surface, image acquisition time was kept below ~6 min. For a typical 60 min electrolysis experiment, this provided at least 10 images. This temporal resolution limited the scan size to approximately 1 × 1 μm; larger scan sizes would have required too fast a tip velocity or taken too long to record. GDEs with a simpler geometry<sup>28</sup> could allow faster tip velocities.

The mechanical flexibility of the GDE also posed a challenge. Since the Bruker Icon electrochemical cell was designed for ~40 × 40 mm samples (electrochemical cell O-ring seal is 36 mm diameter), our initial attempts with GDE samples used 40 × 40 mm GDEs masked with tape except for the small 0.5–1 mm diameter area with catalyst. However, with the GDE anchored to the electrochemical cell a 20 mm radius away from the scan area, adhesion between the AFM probe and GDE would be strong enough, and the GDE flexible enough, that the AFM probe could not detach from the GDE during PF tapping. By reducing the size of the GDE down to 4 × 4 mm, the tape could be secured to the stiff electrochemical cell base 2 mm away from the scan area, which allowed for scanning in PF tapping mode. This design is depicted in the schematic of Fig. 1c. It is important to note that attempts to cut the GDL material smaller than 4 × 4 mm often caused the carbon paper backing to detach from the microporous layer of the GDL.

**EC-AFM measurements.**—Operando EC-AFM observation of a GDE allows the ability to observe morphological catalyst restructuring and precipitate formation to be observed in real-time under high current density operating conditions for GDE-based electrolyzers. Specifically, a macroscopic electrode (GDE diameter 1 mm) with gas flow and a bulk electrolyte (2 ml) can be probed. Local pH gradients similar to those in high performance GDE experiments can form,<sup>26,29</sup> and EC-AFM can measure catalyst changes caused by this high current/potential operation. In future work, liquid flows could be added to the system to further resemble realistic electrolysis operating conditions.

In this work, videos of topography and mechanical property maps were recorded. Image recording rates varied from 6 min per frame (256 × 256 image, 1 × 1 μm scan size, 0.709 Hz scan rate) for Fig. 2 and 7 to ~1 min per frame (256 × 128 image, 1 × 0.5 μm scan size, 2 Hz scan rate) for Fig. 4. Fig. 3 shows frames from a 108 min 1 mA cm<sup>-2</sup> electrolysis and subsequent 60 min 10 mA cm<sup>-2</sup> electrolysis on one Cu-sputtered GDE (see appendix for video of 3d topography images). The potential during each image is circled in the potential vs time plots of Fig. 3, showing the 1 mA cm<sup>-2</sup> cell potential (cathode vs anode) as ~−1.7 V, and the 10 mA cm<sup>-2</sup> as ~−2.7 V. The latter decreased at 55 min to below −4 V, possibly due to flooding of the GDE. Fig. 4 shows frames from a ~4 min 100 mA cm<sup>-2</sup> electrolysis, with cell potential −2.3 to −3.0 V. Cell potential decreased at 2 min 40 s to below −3 V when the AFM probe holder was withdrawn from the GDE by 1 mm in ~1 s; such a shift in potential was common when withdrawing the probe holder, e.g. Fig. A-2, and is likely a consequence of electrolyte agitation. Specifically, since the GDE potential becomes increasingly cathodic after lifting the probe holder, which is characteristic of GDEs when they become flooded, this agitation may initiate GDE flooding.

The sample drift was slow enough in the above measurements that most features stayed within the 1 × 1 μm<sup>2</sup> or 1 × 0.5 μm<sup>2</sup> scan area: from before electrolysis to minute 26 of the 1 mA cm<sup>-2</sup> electrolysis the sample drift was 260 nm (shift mostly at current

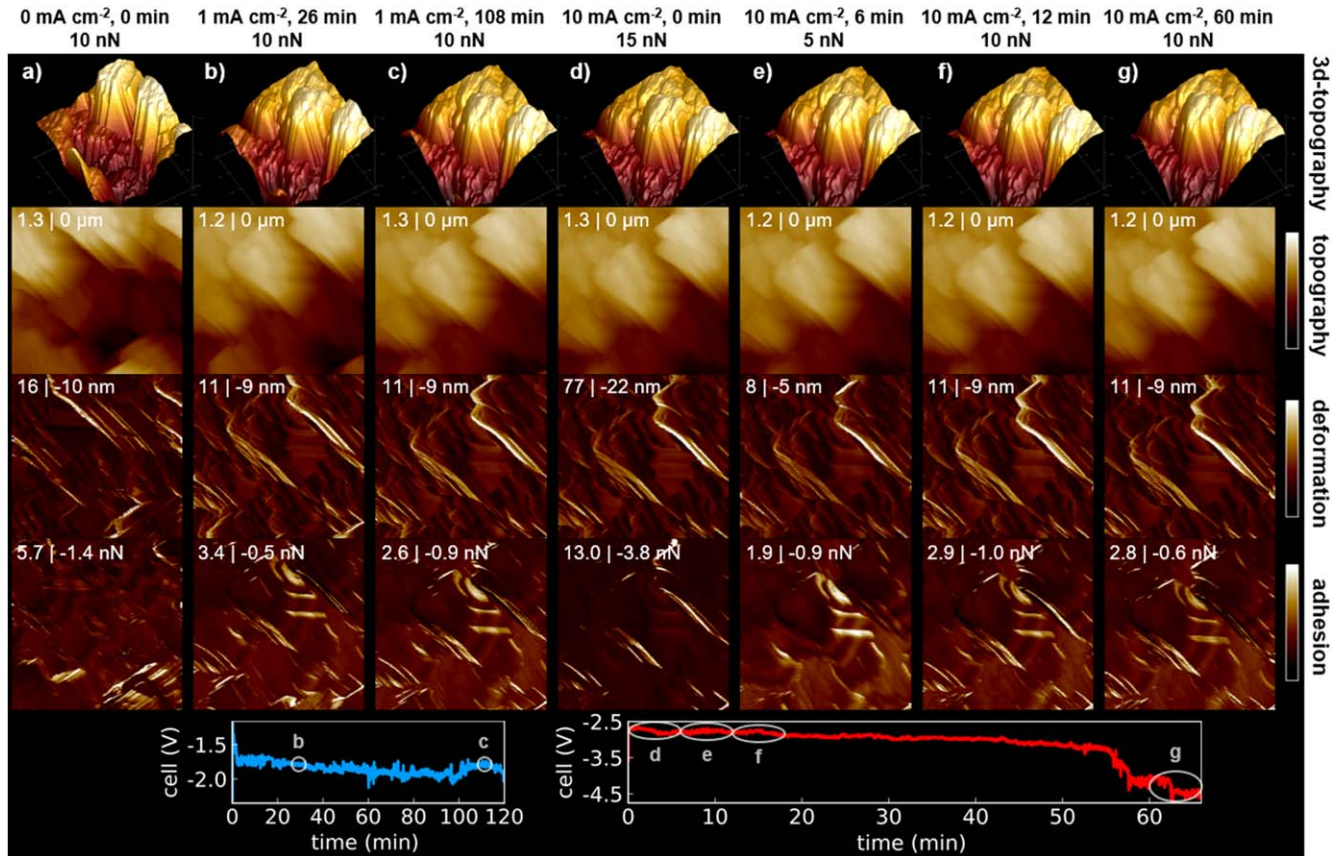


**Figure 3.** EC-AFM images and associated mechanical property maps of Cu-sputtered GDE for 0, 1, and  $10 \text{ mA cm}^{-2}$  at PF tapping set points of 5, 10, and 15 nN. Associated chronopotentiometry below AFM images, with white circles indicating time during each AFM scan; cell potential is cathode vs anode; negative shift in cell potential at 55 min did not affect AFM scanning. Annotations on each image denote the max (white) and min (black) values for the color bar. Scan rate 0.7 Hz. PF tapping frequency 1 kHz. Pixels  $256 \times 256$ . Scan size of all images  $1 \times 1 \mu\text{m}^2$ .

onset). From minute 26 to minute 108 operating at  $1 \text{ mA cm}^{-2}$  the sample drift was only  $100 \text{ nm}$  ( $1.2 \text{ nm min}^{-1}$ ), and from minute 0 to minute 60 of the subsequent  $10 \text{ mA cm}^{-2}$  electrolysis the drift was only  $73 \text{ nm}$  ( $1.2 \text{ nm min}^{-1}$ ). The overarching take-away is that the sputtered Cu films in the GDE had very stable topography and mechanical property maps, with no evidence for restructuring or precipitate formation during operation under the aforementioned operating conditions and times.

To look for evidence of gas bubbles at the catalyst surface, maps of deformation and adhesion were recorded simultaneously to the topography. Deformation is the vertical travel distance of the AFM probe between initial tip-sample contact and the PF tapping force setpoint being reached. Adhesion is the maximum attractive force between tip and sample while the tip is lifted from the sample surface. Previous research has shown gas bubbles pinned to a metal foil surface have a larger deformation than the metal foil, that deformation of bubbles increases with PF tapping setpoint, and that the measured bubble radius shrinks with increasing PF tapping setpoint.<sup>1</sup> Figure 3 shows deformation maps for 0, 1, and  $10 \text{ mA cm}^{-2}$ , with 15, 5, and 10 nN PF tapping setpoint during  $10 \text{ mA cm}^{-2}$ . These data showed no evidence of a liquid-gas interface; no regions of relatively high deformation changed their size, and all these regions aligned with GDE topography features expected to have high deformation due to their mechanical properties. The only effect of increasing PF tapping setpoint was an increase in the limits of the deformation and adhesion color bar, otherwise the maps looked nearly identical.

The features of the GDE that showed characteristic large deformation and adhesion were the edges of catalyst particles. Flat

catalyst particle surfaces had the lowest deformation, and the portion of the topography images in Fig. 3 that showed tip imaging (flat sloping surface between catalyst particles at height  $\sim 0 \mu\text{m}$  to  $\sim 1 \mu\text{m}$ ) had mid-range deformation. Presumably the mid-range and high deformation is from the side of the pyramid-shaped AFM probe contacting a catalyst particle edge and sliding along it until the PF tapping setpoint was reached, causing a larger vertical travel distance between the initial probe-sample contact and reaching PF tapping setpoint.

In the appendix we highlight an example of an artifact typical to the technique. While Fig. 3 showed a very stable topography at 0, 1, and  $10 \text{ mA cm}^{-2}$ , in the magnified view in Fig. A.3 some relatively smooth catalyst particles appeared to break up into smaller grains when a cathodic potential was first applied to the GDE. However, as indicated by the white arrows in Fig. A.3, repeating of features in the  $1 \text{ mA cm}^{-2}$  image suggest the apparent roughness was actually tip-imaging of a particle attached to the AFM probe. The high aspect ratio roughness of the GDE surface makes it especially prone this artifact, and future work with this technique should be mindful of it.

To look for the salt crystal precipitate commonly found post-mortem on  $\text{CO}_2\text{R}$  GDEs,<sup>30–32</sup> a GDE was run at  $10 \text{ mA cm}^{-2}$  for 1 h,  $50 \text{ mA cm}^{-2}$  for 1 h, then rinsed with de-ionized water and dried for 24 h. Salt crystals were apparent on the GDE surface, but covered  $\sim 10 \times 10 \mu\text{m}^2$  areas, with  $5–10 \mu\text{m}$  gaps between the crystals, through which the GDE was exposed. Fig. A.4 shows a  $20 \times 20 \mu\text{m}^2$  topography image of this, suggesting that future work focused on precipitate formation would benefit from large scan sizes to avoid imaging only a gap between crystals.

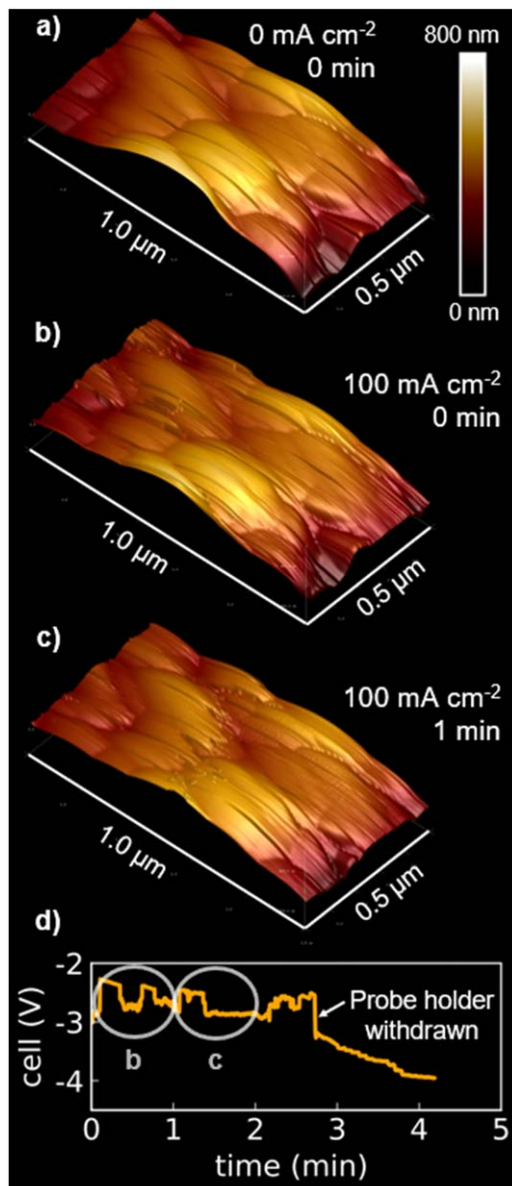


**Figure 4.** EC-AFM images of Cu-sputtered GDE at  $100 \text{ mA cm}^{-2}$ . (a)  $0 \text{ mA cm}^{-2}$ . (b) AFM scan and  $100 \text{ mA cm}^{-2}$  started simultaneously. (c) AFM scan started 1 min after  $100 \text{ mA cm}^{-2}$  was started. Color bar applies to all images. (d) Chronopotentiometry, with white circles indicating time during each AFM scan; cell potential is cathode vs anode; at 2:40 min the AFM probe holder was withdrawn by 1 mm in  $\sim 1$  s. Scan rate 2 Hz. PF tapping frequency 2 kHz. Pixels  $256 \times 128$ . Scan size  $1 \times 0.5 \mu\text{m}^2$ . Images recorded consecutively with  $\sim 1$  s pause between.

To test the limits of this technique, the topography was measured during electrolysis on a Cu-sputtered GDE at  $100 \text{ mA cm}^{-2}$  (cell potential  $-2.3$  To  $-3.0$  V). Figure 4 shows the topography before electrolysis and for the first two minutes of electrolysis. During the third minute, the AFM probe lost contact with the GDE surface and bubble formation in the electrolyte (likely  $\text{O}_2$  generated at the anode) prevented further imaging. The catalyst particles were the round spherical surfaces, and showed no change in topography from the electrolysis. The long narrow streaks in the image are an artifact from vacuum pump vibrations; to prevent gas build-up and associated positive pressure, the vacuum and water bubbler vial (described in the experimental section) were used here. For future work, the BPM suggested above may enable more stable measurements at this high current density.

## Conclusions

In conclusion, we have demonstrated an electrochemical cell design that is able to use EC-AFM to study GDEs for high current density electrolysis. While GDEs exhaust gas products through the gas diffusion media, the new cell design developed in this work enables EC-AFM measurements of  $\text{CO}_2\text{R}$  catalysts at much higher current densities than are possible on the solid electrodes used to date for EC-AFM. Design constraints include small GDL samples ( $4 \times 4 \text{ mm}^2$ ) to securely mount the flexible material and a  $0.5\text{--}1 \text{ mm}$  diameter opening in a  $45 \mu\text{m}$  thick mask on the GDE to maintain low net current and EC-AFM probe access to the GDE through the small mask opening. EC-AFM measurements showed stable topography, adhesion, and deformation maps at 1 and  $10 \text{ mA cm}^{-2}$  and stable topography at  $100 \text{ mA cm}^{-2}$ . Future improvements include electrolyte flow, a BPM to separate the anode and cathode, simpler GDE geometries for faster tip velocities, larger cathodic potentials to investigate catalyst restructuring, and a more basic pH in the catalyst microenvironment to investigate precipitate formation of carbonate and bicarbonate salts.

## Acknowledgments

This work was authored in part by the National Renewable Energy Laboratory (NREL), operated by Alliance for Sustainable Energy, LLC, for the U.S. Department of Energy (DOE) under Contract No. DE-AC36-08GO28308. This work was supported by the Laboratory Directed Research and Development (LDRD) Program at NREL. The views expressed in the article do not necessarily represent the views of the DOE or the U.S. Government. The U.S. Government retains and the publisher, by accepting the article for publication, acknowledges that the U.S. Government retains a nonexclusive, paid-up, irrevocable, worldwide license to publish or reproduce the published form of this work, or allow others to do so, for U.S. Government purposes. This project has received funding from the European Research Council (ERC) under the European Union's Horizon 2020 research and innovation programme (grant agreement no. 759743—WUTANG). The authors thank Marcel Bus of TU Delft for many helpful conversations.

## Appendix

Supplemental experimental setup photographs and schematics.

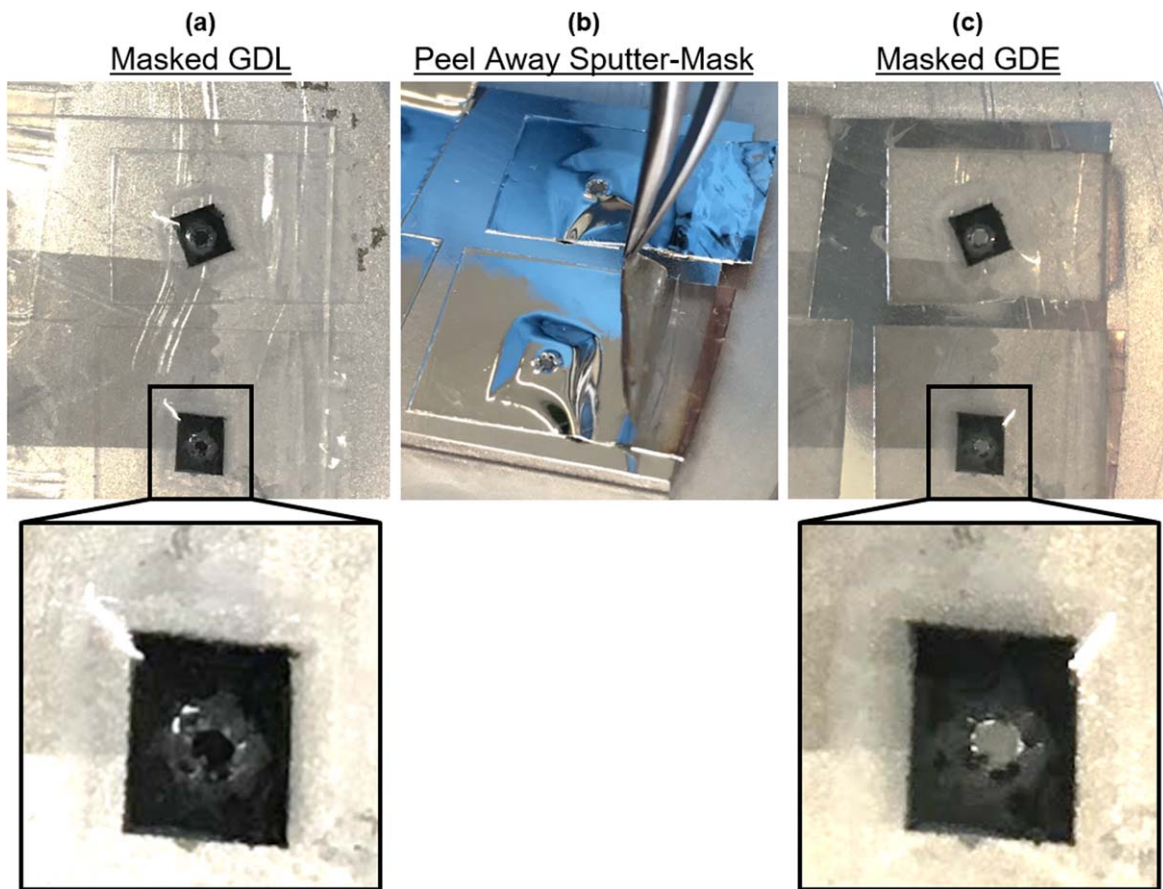


**Figure A-1.** Two layers of tesapack tape on the GDL allow the top layer to act as a sputter mask and be removed after sputtering a catalyst (here Ag). The bottom layer remains on the GDL to mask the GDL from the electrolyte in the electrochemical cell. Black GDE in inset is approximately  $3 \times 4$  mm.

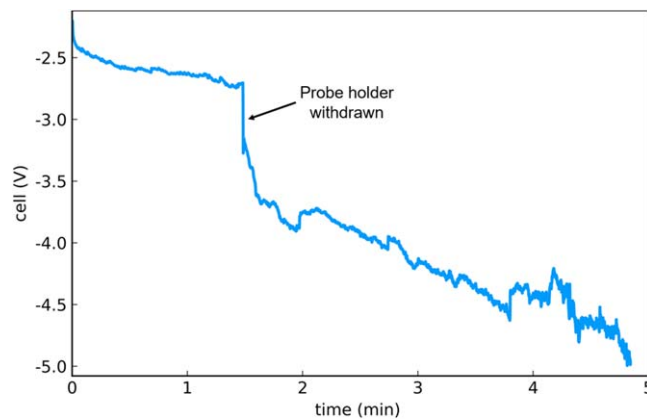


**Figure A-2.** Chronopotentiometry at  $100 \text{ mA cm}^{-2}$  on Cu-sputtered GDE; cell potential is cathode vs anode; at 1:30 min the AFM probe holder was withdrawn by 1 mm.

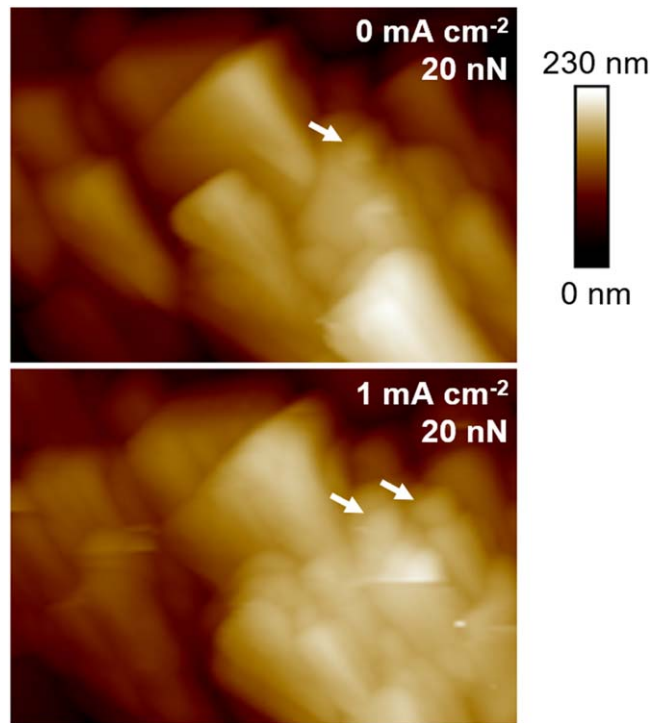


**Figure A3.** Example of artifact in EC-AFM topography of Cu-sputtered GDE for 0 and 1  $\text{mA cm}^{-2}$ . The topography develops numerous ridges from 0  $\text{mA cm}^{-2}$  to 1  $\text{mA cm}^{-2}$ . Since features from the top image can be seen repeated in bottom image, as indicated by white arrows, this apparent roughness is likely an artifact from a particle on the AFM tip. Color bar applies to both images. Scan rate 0.7 Hz. PF tapping frequency 1 kHz. Pixels 256  $\times$  256. Scan size 1  $\times$  1  $\mu\text{m}^2$  (cropped to 500  $\times$  351 nm). Images recorded consecutively with  $\sim$ 1 s pause between; current changed from 0 to 1  $\text{mA cm}^{-2}$  between the scans.

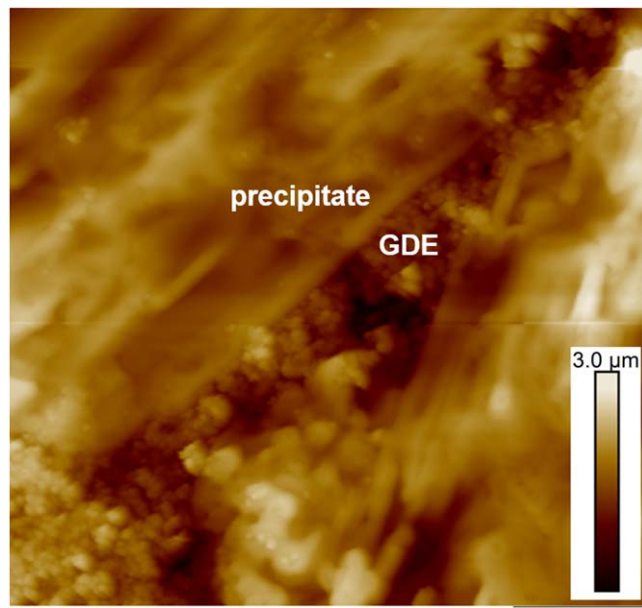


**Figure A4.** Salt precipitate on a Ag sputtered GDE after rinsing and drying the GDE (AFM recorded in air). Annotations show which regions are the salt and which are the GDE. Scan rate 0.5 Hz. Pixels 256  $\times$  256. Scan size 20  $\times$  20  $\mu\text{m}^2$ .

## References

- W. Walczyk, P. M. Schön, and H. Schönherr, *J. Phys. Condens. Matter*, **25**, 184005 (2013).
- F. J. Giessibl, *Surface scanning method*, US7665350B2 (2010).
- B. V. Derjaguin, V. M. Muller, and Y. P. Toporov, *J. Colloid Interface Sci.*, **53**, 314 (1975).
- P. Grossé, D. Gao, F. Scholten, I. Sinev, H. Mistry, and B. Roldan Cuenya, *Angew. Chem. Int. Ed.*, **57**, 6192 (2018).
- S. V. Kalinin et al., *ACS Nano*, **13**, 9735 (2019).
- M. R. Nellist, J. Qiu, F. A. L. Laskowski, F. M. Toma, and S. W. Boettcher, *ACS Energy Lett.*, **3**, 2286 (2018).
- S. Kim, K. No, and S. Hong, *Chem. Commun.*, **52**, 831 (2016).
- S. Kalinin, N. Balke, S. Jesse, A. Tselev, A. Kumar, T. M. Arruda, S. Guo, and R. Proksch, *Mater. Today*, **14**, 548 (2011).
- S. Nagamatsu, T. Arai, M. Yamamoto, T. Ohkura, H. Oyanagi, T. Ishizaka, H. Kawanami, T. Uruga, M. Tada, and Y. Iwasawa, *J. Phys. Chem. C*, **117**, 13094 (2013).
- S. Popović, M. Smiljanić, P. Jovanović, J. Vavra, R. Buonsanti, and N. Hodnik, *Angew. Chem. Int. Ed.*, **59**, 14736 (2020).
- A. Bergmann and B. Roldan Cuenya, *ACS Catal.*, **9**, 10020 (2019).
- G. L. De Gregorio, T. Burdyny, A. Lojudice, P. Iyengar, W. A. Smith, and R. Buonsanti, *ACS Catal.*, **10**, 4854 (2020).
- T. Masuda, K. Ikeda, and K. Uosaki, *Langmuir*, **29**, 2420 (2013).
- C. Liu and S. Ye, *J. Phys. Chem. C*, **120**, 25246 (2016).
- I. Khalakhan, M. Vorokhta, P. Kúš, M. Dopita, M. Václavů, R. Fiala, N. Tsud, T. Skála, and V. Matolín, *Electrochim. Acta*, **245**, 760 (2017).
- I. Khalakhan, A. Choukourov, M. Vorokhta, P. Kúš, I. Matolínová, and V. Matolín, *Ultramicroscopy*, **187**, 64 (2018).
- S. Manne, P. K. Hansma, J. Massie, V. B. Elings, and A. A. Gewirth, *Science*, **251**, 183 (1991).
- Q. Xu, E. Kreidler, and T. He, *Electrochim. Acta*, **55**, 7551 (2010).
- Y.-G. Kim, J. H. Baricuatro, A. Javier, J. M. Gregoire, and M. P. Soriaga, *Langmuir*, **30**, 15053 (2014).
- R. Reske, H. Mistry, F. Behafarid, B. Roldan Cuenya, and P. Strasser, *J. Am. Chem. Soc.*, **136**, 6978 (2014).
- H. Xiang, S. Rasul, K. Scott, J. Portoles, P. Cumpson, and E. H. Yu, *Journal of CO2 Utilization*, **30**, 214 (2019).
- S. Hernandez-Aldave and E. Andreoli, *Catalysts*, **10**, 713 (2020).
- M. König, J. Vaes, E. Klemm, and D. Pant, *iScience*, **19**, 135 (2019).

## ORCID

Nathan T. Nesbitt <https://orcid.org/0000-0002-1806-1077>  
Wilson A. Smith <https://orcid.org/0000-0001-7757-5281>

24. T. Haas, R. Krause, R. Weber, M. Demler, and G. Schmid, *Nat. Catal.*, **1**, 32 (2018).
25. Y. C. Li, D. Zhou, Z. Yan, R. H. Gonçalves, D. A. Salvatore, C. P. Berlinguet, and T. E. Mallouk, *ACS Energy Lett.*, **1**, 1149 (2016).
26. C.-T. Dinh et al., *Science*, **360**, 783 (2018).
27. K. Liu, W. A. Smith, and T. Burdyny, *ACS Energy Lett.*, **4**, 639 (2019).
28. W. V. Fernandez, R. T. Tosello, and J. L. Fernández, *Analyst*, **145**, 122 (2019).
29. T. Burdyny and W. A. Smith, *Energy Environ. Sci.*, **12**, 1442 (2019).
30. E. W. Lees, B. A. W. Mowbray, D. A. Salvatore, G. L. Simpson, D. J. Dvorak, S. Ren, J. Chau, K. L. Milton, and C. P. Berlinguet, *J. Mater. Chem. A*, **8**, 19493 (2020).
31. S. Verma, Y. Hamasaki, C. Kim, W. Huang, S. Lu, H.-R. M. Jhong, A. A. Gewirth, T. Fujigaya, N. Nakashima, and P. J. A. Kenis, *ACS Energy Lett.*, **3**, 193 (2018).
32. J.-J. Lv, M. Jouny, W. Luc, W. Zhu, J.-J. Zhu, and F. Jiao, *Adv. Mater.*, **30**, 1803111 (2018).